Astronomy & Astrophysics manuscript no. J0522-364-alma-astroph
October 27, 2015
©ESO 2015

Anatomy of a blazar in the (sub-)millimeter: ALMA Observations of *PKS 0521-365*

S. Leon[1], P. C. Cortes[1,5], M. Guerard[1], E. Villard[1], T. Hidayat[2], B. Ocaña Flaquer[3], B. Vila-Vilaro[1]

[1] Joint ALMA Observatory - ESO, Av. Alonso de Córdova, 3104, Santiago, Chile
[2] Bosscha Observatory and Astronomy Research Division, FMIPA, Institut Teknologi Bandung, Indonesia
[3] CAUP, Porto University, Portugal
[4] Instituto de Astrofísica de Andalucía-CSIC, Granada, Spain
[5] National Radio Astronomy Observatory, 520 Edgemont Rd, Charlottesville, VA, 22903, USA

Received September 15, 1996; accepted March 16, 1997

arXiv:1510.07536v1 [astro-ph.GA] 26 Oct 2015

ABSTRACT

Aims. We aim at analyzing the (sub-)millimeter emission in a nearby blazar, *PKS 0521-365*, to study the synchrotron and thermal emission in the different components detected at low frequency.
Methods. We analyze the archive public data of the ALMA Cycle 0 where *PKS 0521-365* is used as a calibrator. A total of 13 projects with 23 dataset is analyzed in band 3, 6 and 7 and combined. The whole set of data is combined and wavelet filtered to obtain a deep image towards *PKS 0521-365* reaching a dynamic range of 47000. The individual emission flux is measured at different date over a period of 11 months in various components. Finally we analyze the Spectral Energy Distribution (SED) in each different component, including the radio jet and counter jet.
Results. The point sources detected in the field follow a similar distribution to previous studies. The blazar flux shows large variation especially in band 3. Different components are observed: core, radio jet and newly detected counter jet, Hot Spot (HS) and a disky structure roughly perpendicular to the jet. The HS emission is formed by a point source surrounded by an extended emission. The viewing angle of the jet is about 30° with a Doppler factor of $\delta = 1.6$. The HS is at a distance of 19 kpc from the center. The SED analysis shows a strong variation of the core spectral index, especially in band 3. The two components in the radio jet have roughly a flat spectral index in band 6 and 7.
Conclusions. Using these ALMA data the different weak and extended components in *PKS 0521-365* are detected. The analysis of both jets constrains the geometrical distance of the HS to the center. The SED presents a different shape in time and frequency for each component. Finally a new structure is detected roughly perpendicular to the radio jet and a thermal emission origin is currently favoured. Further observations at higher spatial resolution are needed to confirm that hypothesis.

Key words. galaxies: jets – galaxies: ISM – galaxies: active – galaxies: BL Lacertae objects: *PKS 0521-365*

1. Introduction

Inside the large range of different type of active galactic nuclei (AGN) blazars are the most powerful sources. Showing intense emission across the electromagnetic spectrum, it is thought that this strong continuum emission is due to an ejection of relativistic plasma nearly on the line of sight. A radio jet is commonly observed in blazars at lower frequencies (Antonucci & Ulvestad, 1985) and their strong flux is accounted for the relativistic beaming. A blazar is then a particular case of a head-on radio galaxy from an underlying population with a spread geometry distribution of the jet (Antonucci & Ulvestad, 1985; Urry & Padovani 1995) originating from an AGN and oriented nearly head-on towards the observer according to the unified scheme proposed two decades ago (e.g. Urry & Padovani, 1995). The jet can be detected up to large energy ranges (Gamma, X-ray) because of the strong beaming effect. Blazars can be divided into two types, the low power AGNs, mainly without Broad-Line Regions (BLRs) and a large synchrotron break frequency (Capetti et al. 2010, Tavecchio et al. 1998), and the Flat-Spectrum Radio Quasars (FSRQs) with a lower break frequency (Maraschi & Tavecchio 2003). The first kind forms the family of BL Lac radio galaxies which was the first of its kind detected (e.g. Blandford & Rees 1978). The SED of the blazar shows normally two bumps, the synchrotron bump at low energy peaking in the infrared (IR)-X-ray and the Inverse Compton (IC) bump normally in γ-ray. Each bump is characterized by a peak frequency ν_1 and ν_2 at the peak of the emission in each regime. Fossati et al. (1998) found an anti-correlation between the peak frequency ν_1 and the bolometric and synchrotron luminosity. They suggested a link between the source power and the frequency peak. The sequence may match a spectroscopic one, from powerful FSRQ sources at the low-peak, high-luminosity end and the BL Lacs with high-peak and low-luminosity. The BL Lacs do not show normally signs of BLRs. It was suggested that the Inverse Compton (IC) emission in FSRQ was produced through the Synchrotron Self Compton (SSC) mechanism or from external seed photons from the BLRs. These photons would be up-scattered by the synchrotron electrons (e.g. Chen et al. 2012). The long-standing Unified Scheme for radio-loud AGN proposes that the Fanaroff-Riley I and II radio galaxies (Fanaroff & Riley, 1974) are the underlying progenitors of BL Lacs and FSRQs galaxies (Bicknell 1995, Fossati et al. 1998).

In a population synthesis study, Lister & Marscher (1997) used realistic luminosity functions to show that the majority of compact extragalactic radio sources have jets with low Lorentz factors. The AGN in general and the jet in particular are known

to drive the evolution of their host galaxy (Best & Heckman 2012, Khalatyan et al. 2008, Sturm et al. 2011) through a feedback mechanism of depositing energy in the interstellar medium (ISM). At large scale the radio jet can slow down or stop the cooling of the massive X-ray halo (Fabian 2012) that surrounds these galaxies. At the galactic scale the jet interacts with the local ISM (molecular gas, X-ray halo, etc), and it has been suggested that for host galaxies with a dense ISM phase the radio jet could be completely confined to the central part with no outwards propagation (Carvalho 1998) forming Compact Steep Spectrum galaxies. It was argued recently (Rashed et al., 2013) that the backflow along the radio jet in the elliptical host galaxy SDSS J080800.99+483807.7 might have triggered star formation. This star formation triggering mechanism in radio galaxies has been used to explain the correlation between the radio and optical morphologies of distant 3C radio galaxies (McCarthy et al., 1987). Some of the most dramatic jet-induced star formation, with star formation rates (SFR) as high as 1000 $M_{\odot}\mathrm{yr}^{-1}$, is associated with very luminous radio galaxies at redshifts up to $z \sim 4$ (Dey et al. 1997; Bicknell et al. 2000).

One study has found a clear interaction of the radio jet and the ISM in the Narrow Line Regions (NLRs) of Seyfert galaxies (Falcke et al., 1998). Such interactions play a major role in determining the morphology of the NLR, as the radio jets sweep up and compress ambient gas, producing ordered structures with enhanced surface brightness in line emission. The nearby radio galaxy M 87 which can be classified as a BL Lac was recently found to have a giant radio-to-X-ray synchrotron (Stawarz et al., 2006). It was argued that the presence of a gaseous concentration in the central part would provoke the interaction of the jet with such a feature resulting in the formation of a stationary shock structure in the innermost parts of the M 87 jet.

The radio source *PKS 0521-365* (J0522-364) is a nearby AGN (Danziger et al. 1979) and it is one of the most remarkable extragalactic objects of the southern sky, because it exhibits a variety of nuclear and extra-nuclear phenomena. In this work we assume a cosmology with $\Omega_m = 0.27$, $\Omega_\Lambda = 0.73$, $H_0 = 71$ km s^{-1} Mpc^{-1} (Spergel et al. 2003). At $z = 0.0565$, *PKS 0521-365* is at a comoving radial distance of 236 Mpc, and have a linear scale size of 1.15 kpc/arcsec. Classified as a BL Lac object, it shows strong narrow and broad emission lines typical of type 1 AGN both in the optical and the UV (Ulrich 1981; Danziger et al. 1983; Scarpa et al. 1995). The source has a prominent radio, optical, and X-ray jet (Danziger et al. 1979; Keel 1986; Falomo 1994; Macchetto et al. 1991; Scarpa et al. 1999; Birkinshaw et al. 2002), which resembles that of the nearby radio galaxy M 87 (Sparks et al. 1994).

Here we present archival ALMA observations of the radio source *PKS 0521-365*. We retrieved public Cycle-0 observation where *PKS 0521-365* was used as calibrator in band 3, 6, and 7. Section 2 presents the observations and data reduction, section 3 the millimeter and sub-millimeter distribution of the emission, section 4 the variability in the emission, section 5 computes the spectral index, section 6 the discussion, and section 7 the summary and conclusions.

2. Observations and data reduction

Publicly available data from ALMA Cycle 0 observations were used to analyze the sub-millimeter properties of the blazar *PKS 0521-365*. As shown on Table 1 the observations span a period of about 1 year from 2012/01/10 to 2012/11/19. The observed frequencies go from 87.3 GHz up to 372.5 GHz, which covers bands 3, 6 and 7. *PKS 0521-365* was generally used as a bandpass calibrator for the science projects sharing the same spectral setup, and observed between 2 to 4 minutes per execution. If two ExecBlocks (hereafter EBs) were observed consecutively, we merged them in a single dataset and the observing time was chosen as the starting time of the first EB. Each EB has four spectral windows of, generally, 2 GHz bandwidth distributed over 4 basebands, two in the USB window and two in the LSB window. For the flux determination of each dataset the four spectral windows were combined and the LSB/USB spectral windows were used to determine the spectral index α, hereafter defined as $S_\nu \propto \nu^\alpha$ with S_ν the flux density at the frequency ν, in one dataset as indicated further. Before combining the different dataset in each band, a self-calibration was performed on each of them to improve the phase/amplitude gain solutions thanks to the strong continuum emission. The effective frequency quoted for the combined bands was computed using the deconvolution CLEAN task in CASA with the multi-frequency synthesis (mfs) mode, see Rau & Cornwell (2011) for details.

The two most prominent feature of *PKS 0521-365* are the strong core and the so-called "Hot Spot" (HS) located at 8.6″at the South-East of the core. The main properties of each dataset and the measured flux of the core and the Hot Spot are summarized in Table 2. For the core the flux in the central area was measured directly since the jet contribution is less than 1% of the total flux. The HS flux was measured including the pixels above 3-σ of the RMS in the HS area.

The self-calibrated datasets were combined in each band and imaged. A final superset of all self-calibrated dataset, called "band 3+6+7", was created and imaged to produce the most sensitive continuum image at an effective frequency of 221.02 GHz. The total integration time is of 1.55 hours with an equivalent of 66 pad positions and 2145 baselines. The self-calibration of these data allowed us to achieve a RMS noise of 158 μJy for the band 3+6+7 with a dynamic range (SNR) of 27100 without wavelet filtering. The final spatial resolution with a natural weighting is of $0.53'' \times 0.71''$. It is worth noting that the band 7 combined image has the deepest sensitivity (91 μJy) which is similar to the all-in-one combined data. The properties of the combined dataset in band 3, 6, 7 and 3+6+7 are summarized in Table 3 together with the Hot Spot flux which is not varying with time. Each band reaches an effective bandwidth of 27 GHz (band 3) to 285 GHz (band 3+6+7). The effects of the lowest spatial frequencies observed at the different bands was checked by computing the flux of the HS in band 3 using the spatial frequencies of band 7. The HS flux is in that case lower by 5% compared to the measured flux with the full uv-coverage. Given the calibration uncertainty we can assume safely that the differential sensitivity to spatial scales between bands is negligible in the case of the observations of *PKS 0521-365*.

2.1. Wavelet filtering

The wavelet transform is a powerful signal processing technique which provides a decomposition of the signal into elementary local contribution labeled by a scale parameter (Grossman & Morlet 1985). They are the scalar products with a family of shifted and dilated functions of constant shape called wavelets. The data are unfolded in a space-scale representation which is invariant with respect to dilation of the signal. Such an analysis is particularly suited to study signals which exhibit space-scale discontinuities and/or hierarchical features.

The wavelet analysis of the *PKS 0521-365* datasets is performed on the combined dataset in each band after the deconvolution process using the CLEAN algorithm with natural weighting. As

Table 1. Journal of the observations

Id	Project UID	Date	Frequency (GHz)	Integration (seconds)
J0522-364_99_1	2011.0.00099.S	2012/04/06 22:19	98.7/110.3	123
J0522-364_99_2	2011.0.00099.S	2012/07/04 11:53	98.7/110.3	110
J0522-364_99_3	2011.0.00099.S	2012/07/03 11:25	100.6/112.5	171
J0522-364_131_1	2011.0.00131.S	2012/01/24 23:20	101.4/114.5	296
J0522-364_467_1	2011.0.00467.S	2012/03/27 21:23	96.5/108.3	175
J0522-364_108_3	2011.0.00108.S	2012/07/29 10:35	87.3/99.0	233
J0522-364_268_1	2011.0.00268.S	2012/01/10 21:55	252.8/241.3	200
J0522-364_268_2	2011.0.00268.S	2012/01/13 02:26	252.8/241.3	200
J0522-364_210_1_2	2011.0.00210.S	2012/08/09 09:58	219.7/231.2	463
J0522-364_210_3	2011.0.00210.S	2012/08/26 09:14	219.7/231.2	236
J0522-364_108_1	2011.0.00108.S	2011/11/05 06:51	342.8/354.3	115
J0522-364_108_2	2011.0.00108.S	2011/11/06 02:05	342.8/354.3	115
J0522-364_397_1	2011.0.00397.S	2011/11/16 05:24	339.0/351.0	141
J0522-364_124_1_2	2011.0.00124.S	2012/07/18 09:41	318.1/330.1	464
J0522-364_768_1	2011.0.00768.S	2012/07/31 09:54	339.8/351.7	175
J0522-364_768_2_3	2011.0.00768.S	2012/08/14 09:15	339.8/351.7	351
J0522-364_83_1	2011.0.00083.S	2012/06/16 11:25	342.8/354.7	326
J0522-364_83_2	2011.0.00083.S	2012/06/17 11:43	342.8/354.7	326
J0522-364_83_3	2011.0.00083.S	2012/08/27 06:59	342.8/354.7	326
J0522-364_208_1	2011.0.00208.S	2012/10/22 03:56	342.4/354.4	200
J0522-364_223_1	2011.0.00223.S	2012/10/21 06:21	330.8/345.6	342
J0522-364_223_2	2011.0.00223.S	2012/10/22 05:08	330.8/345.6	342
J0522-364_340_1_2	2011.0.00340.S	2012/11/19 07:36	358.0/372.5	130

Table 2. Dataset properties (natural weighting)

Id	MJD	ν_{eff} (GHz)	Beam (arcsec)	RMS (mJy)	Flux (Core) (mJy)	Flux (HS) (mJy)
J0522-364_99_1	56023.93	104.55	1.34×1.72	3.9	7174	83
J0522-364_99_2	56112.50	104.33	1.69×2.41	3.0	6111	178
J0522-364_99_3	56111.48	106.62	1.43×2.46	0.6	4858	163
J0522-364_131_1	55950.97	107.99	3.14×4.46	1.4	5317	142
J0522-364_467_1	56013.89	102.40	1.47×1.69	3.0	9623	133
J0522-364_108_3	56137.44	93.16	1.52×2.64	1.3	5474	177
J0522-364_268_1	55936.91	247.08	1.32×2.68	2.1	4208	33
J0522-364_268_2	55939.10	247.08	1.19×1.78	1.0	4524	44
J0522-364_210_1_2	56148.42	225.43	0.67×0.91	0.3	4732	53
J0522-364_210_3	56165.38	225.44	0.68×0.97	0.7	4735	52
J0522-364_108_1	55870.29	348.58	1.18×1.35	0.7	5345	17
J0522-364_108_2	55871.09	348.58	1.17×2.95	0.6	5077	14
J0522-364_397_1	55881.22	344.99	1.23×1.39	0.9	5254	19
J0522-364_124_1_2	56126.40	324.15	0.43×0.80	0.3	3310	25
J0522-364_768_1	56139.41	345.77	0.41×0.75	1.8	3973	22
J0522-364_768_2_3	56153.39	345.77	0.45×0.66	0.2	4087	23
J0522-364_83_1	56094.48	348.82	0.58×0.91	0.6	4870	21
J0522-364_83_2	56095.49	348.82	0.47×0.82	0.8	4683	26
J0522-364_83_3	56166.29	348.82	0.44×0.95	4.1	3733	31
J0522-364_208_1	56222.16	348.42	0.52×0.79	0.5	4245	26
J0522-364_223_1	56221.26	338.19	0.51×0.60	0.3	4518	24
J0522-364_223_2	56222.21	338.19	0.52×0.63	0.4	4588	19
J0522-364_340_1_2	56250.32	365.28	0.50×0.61	0.9	7666	10

described in Leon et al. (2000) we use the "A trous" algorithm (see Bijaoui 1991). It allows to get a discrete wavelet decomposition within a reasonable CPU time. The kernel function $B_s(x, y)$ for the convolution is a B_3 spline function.

The wavelet transform (WT) $W(i, x, y)$ of the image $I(x, y)$ is then obtained from the following steps:

$$c_o(x, y) = I(x, y), \quad (1)$$

$$c_i(x, y) = c_{i-1} * B_s(\frac{x}{2^i}, \frac{y}{2^i}), \quad (2)$$

$$W(i, x, y) = c_i(x, y) - c_{i-1}(x, y). \quad (3)$$

Table 3. Sets of combined data (natural weighting) together with the Hot Spot flux. The properties indicated are with the wavelet filtering. See text for more details.

Set	ν_{eff} (GHz)	Beam (arcsec)	RMS (μJy)	Dynamic Range	Flux (HS) (mJy)
band 3	100.43	1.59×2.49 (PA=78°)	306	15300	153
band 6	237.06	0.69×0.93 (PA=93°)	147	28500	39
band 7	336.44	0.48×0.64 (PA=90°)	91	40000	22
band 3+6+7	221.02	0.53×0.71 (PA=90°)	90	47000	43

The last plane, called Last Smoothed Plane (LSP), is the residuals of the last convolution and not a wavelet plane, but for convenience we will speak of wavelet plane for all these planes. Each plane $W(i, x, y)$ represents the details of the image at the scale i. A wavelet plane i has a spatial resolution of 0.86×2^i pixels which translates into $0.21''$ in band 3 and $0.08''$ in band 6, 7 and combined for the wavelet plane 0.
Then each component of the raw map $W(i, x, y)$ was filtered, above a given threshold β, using the RMS noise σ_i on each wavelet scale i to get the filtered wavelet planes $W_f(i, x, y)$ of the radio continuum distribution in the different bands:

$$\begin{aligned} W_f(i,x,y) &= W(i,x,y) \quad \text{If } |W(i,x,y)| > \beta\sigma_i \\ &= 0 \qquad\qquad \text{Otherwise} \end{aligned}$$

In this study the wavelet coefficients are filtered at the 4.5-σ level. After WT filtering for the continuum distribution in the different bands the actual dynamic range increases in the different filtered set of data. Thus the combined band 3+6+7, after WT filtering, has a dynamic range of 47000 and the combined band 7 reaches a dynamic range of 40000. By combining the wavelet scales one can achieve a different spatial resolution with a specific RMS noise. Since the contribution of an image I is spread over the different spatial scales, the reconstruction through a limited set of wavelet scales is a lower limit to the total emission contribution. That effect is visible in Table 4 where the core flux is computed for the different wavelet reconstructions. A final equivalent RMS noise of 90 μJy can be achieved for the band 3+6+7. It is worth noting that the "A trous" wavelet decomposition is not strictly orthogonal and the spatial scale contribution can be spread over different wavelet scales. But the algorithm has a quasi-isotropic kernel which makes the physical analysis of each scale easier to perform. In our notation of the WT for the continuum images the scale 0 has the highest spatial resolution and the scale 7 is the LSP. The maximum scale was chosen to be 7 since largest wavelet scales are not giving fundamental informations.

3. (Sub-)millimeter distribution

In order to analyze the sub-millimeter emission towards *PKS 0521-365* the point source distribution was searched in that field. The point sources were searched in the band 3+6+7 WT-filtered field with an effective RMS noise of 90 μJy. The list of the point sources was obtained by using the SExtractor software (Bertin & Arnouts, 1996) at a 4.5-σ level with a minimum of 5 pixels per sources to avoid spurious detections. A total of 16 sources are detected in a $1' \times 1'$ box and their properties are listed in Table 5. Few sources are associated with the continuum emission in *PKS 0521-365* and most of them should be related with background sources as shown on Figure 1. A comparison of the maximum peaks detected in the psf image was done with the point sources and no correlation was found. The source #10 and #12 are respectively associated with the core and the HS emission. It is important to note that the spatial distribution of these sources are not clustered on the radio continuum emission of *PKS 0521-365* but rather uniform through the band 3+6+7 field. Because of the RMS noise of 90 μJy in the WT-filtered band 3+6+7 field we can estimate the number of sources with a flux greater than 0.5 mJy to be $S(> 0.5\text{mJy}) \sim 5760\,\text{deg}^{-2}$. An estimation of the cumulative count at 221 GHz is given on Figure 2 between a flux of 0.1 mJy and 3 mJy. This estimation is not addressing entirely the completeness of the detection and the possible spurious detections and bias. But we note that this estimation is similar, but lower, to the one derived by Hatsukade et al. (2013) using ALMA fields at 238 GHz. Figure 3 shows the band 6 and 7 emission by selecting the wavelet planes 2 to 4 which biases the slightly extended emission. The analysis of the point sources is beyond the scope of this article.

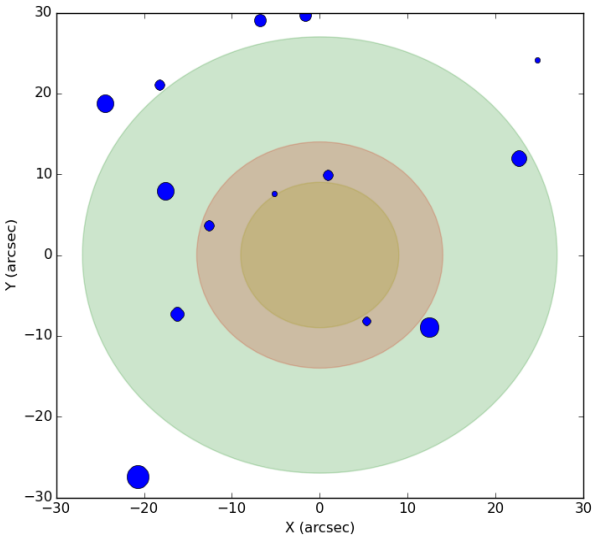

Fig. 1. Point sources detected in the combined field of band 3, 6 and 7 (ν_{eff} = 221.02 GHz) after WT filtering at 4.5σ. The symbols are proportional to the flux. The field is centered on *PKS 0521-365*. The colored circles represent the primary beamsize of each band.

In Figures 4, 5, 6 the WT-filtered emission is shown towards *PKS 0521-365* in band 3 (100 GHz), band 6 (237 GHz) and band 7 (336 GHz). Figure 7 shows the full WT-filtered combined dataset in band 3+6+7. The radio continuum emission shares common features in the three bands: a strong core emission, a radio jet oriented in the N-W direction with a $PA \sim 126°$, a Hot Spot in the symmetric direction of the jet and an elongated jet-like feature close to the nucleus and nearly perpendicular to the main jet with a $PA \sim 66°$. That latter feature is more visible in band 6 and 7 than in band 3 mainly because of the better spatial resolution. The main jet has a length of $6.8''$, i.e. 7.7 kpc in projection at the distance of *PKS 0521-365*. The jet-like feature has a quite sym-

Table 4. Properties of different wavelet reconstruction of the band 3+6+7 combined and WT filtered at 4.5-σ. In our notation the scale 7 is the LSP (see text).

Wavelet Planes	RMS (μJy)	Core Flux (%)
6 - 7	3.7	60
5 - 7	17.3	68
4 - 7	38.9	77
3 - 7	64.8	86
2 - 7	99.3	95
1 - 7	107.9	100

Table 5. Properties of the point sources detected in the band 3+6+7 (ν_{eff} = 221.02 GHz) at a 4-σ level in a box of $1' \times 1'$. The X, Y spatial positions are relative to the nucleus of *PKS 0521-365*. The spatial resolution of the band 3+6+7 dataset is $0.53'' \times 0.71''$.

Id	α_{2000} (degree)	δ_{2000} (degree)	X ($''$)	Y ($''$)	Flux (mJy)	Flux Error (mJy)	FWHM ($''$)
1	80.7422245	-36.4503386	-1.7	29.7	1.05	0.05	0.59
2	80.7440029	-36.4505140	-6.9	29.1	1.06	0.05	0.51
3	80.7331005	-36.4518921	24.7	24.1	0.58	0.03	0.35
4	80.7479270	-36.4527443	-18.2	21.1	0.80	0.04	0.44
5	80.7500829	-36.4533700	-24.5	18.8	1.50	0.05	0.55
6	80.7338043	-36.4552554	22.7	12.0	1.39	0.06	0.66
7	80.7413304	-36.4558385	0.9	9.9	0.85	0.04	0.49
8	80.7476982	-36.4563809	-17.5	8.0	1.50	0.06	0.62
9	80.7434403	-36.4564975	-5.2	7.6	0.57	0.03	0.35
10	80.7415967	-36.4585668	0.1	0.1	4302.94	0.07	0.66
11	80.7460065	-36.4575836	-12.7	3.6	0.84	0.04	0.44
12	80.7440576	-36.4598546	-7.0	-4.5	45.47	0.11	0.98
13	80.7472396	-36.4606248	-16.2	-7.3	1.12	0.05	0.51
14	80.7397929	-36.4608532	5.3	-8.1	0.72	0.04	0.35
15	80.7373352	-36.4610799	12.5	-8.9	1.64	0.05	0.55
16	80.7487821	-36.4662021	-20.7	-27.4	1.97	0.07	0.87

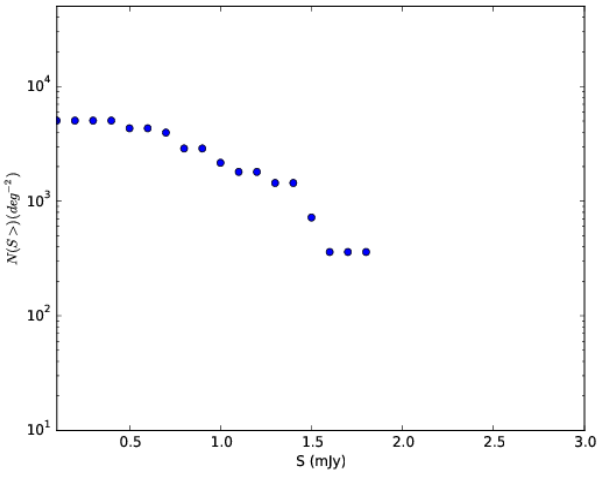

Fig. 2. Cumulative number count at 221 GHz in a field of $1' \times 1'$ between a flux of 0.1 mJy and 3 mJy. The effective RMS noise in the WT-filtered image is 100 μJy.

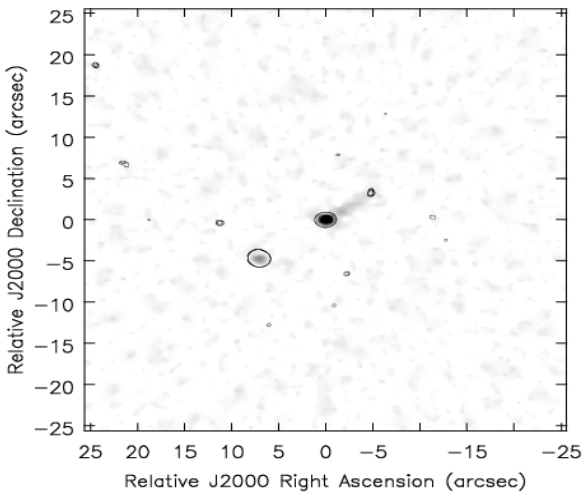

Fig. 3. Contour levels at [4, 4.5, 5, 5.5, 6]-σ of the B6+B7 WT for the scales 2 to 4. The image is the band 7 emission.

metric feature with a length of about $2.6''$(2.9 kpc) in each direction. In band 6 the counter-jet is visible towards the S-E with a length of $3.9''$(4.4 kpc). It is probably visible as well in band 3 but the poorer spatial resolution is not good enough. Because of the dimming at high frequency the counter-jet is not detected so clearly in band 7. We discuss below the comparison between the jet and counter-jet. In band 6 and 7 the Hot Spot is spatially resolved with some extended emission as it was checked by re-

moving a Gaussian component fitted on the Hot Spot and is indicated by the FWHM of the source #36 detected by SExtractor (see Table 5). Inside the jet two main spots, dubbed A and B, are visible and were already detected in different wavelengths (Tingay & Edwards 2002, and references therein). Together with the HS we give their coordinates in Table 6 and their positions in Figure 7. We discuss hereafter the diffuse emission outside of the nucleus, jet and HS which should trace the interaction of the jet with the local interstellar medium.

As indicated before, the WT-filtered decomposition allows to analyze the emission present at specific scales. On Figure 8 the emission in band 3+6+7 at different scales is restored using the WT-filtered decomposition. The most emphasized features using that technique are the counter-jet emission and the extended emission of the HS. The discrete emission outside the central part is emphasized too in the different reconstructions and its relevance was partially addressed before for the low brightness emission in band 6 and 7 using the wavelet planes 2 to 4 (see Figure 3) which select the spatial range 0.4″-1.4″(see Leon et al., 2000), i.e. 450-1600 pc in the galaxy *PKS 0521-365*.

Because of the small viewing angle of the radio jet in blazar and in particular in *PKS 0521-365* the relativistic beaming enhances the approaching blobs of plasma and dims the receding plasma. The counter-jet is then more visible at low frequencies as it is observed here in *PKS 0521-365* (see Table 7). Because of the low spatial resolution in band 3 we searched for the counter-jet emission by using uniform weights during the imaging step achieving detection in only 3 datasets. In band 6, 4 datasets reveal the counter-jet emission and because of its low brightness, the uncertainty on its flux is quite large. To compute the jet/counter-jet emission ratio we use the band 6 estimation with a better spatial resolution, i.e the band 3+6+7 dataset which have an effective frequency in band 6 and a low RMS noise. The jet and counter-jet flux was estimated by subtracting to the image a Gaussian source fitting the nucleus and selecting a polygonal area on the jet and the counter-jet. The emission ratio between the jet and the counter-jet was found to be $\Re = 10.2$.

Assuming an equal intrinsic emission between the jet and the counter-jet, the ratio J between both componet can be estimated as following (e.g. in Ghisellini et al. 1993):

$$J = \left(\frac{1+\beta\cos\theta}{1-\beta\cos\theta}\right)^{p} \quad (4)$$

where β is the bulk velocity expressed in units of the speed of light, θ is the viewing angle and p can be expressed in the simplest cases as $p = 2+\alpha$ (a moving isotropic source) or $p = 3+\alpha$ (a continuous jet) with α the spectral index of the jet. On Figure 9 the ratio J is shown for different bulk velocities taking an intermediate exponent $p = 2.5$ which is used for the analysis. To match the *PKS 0521-365* ratio it appears that the viewing angle must be in the range $\theta \subset [16°, 38°]$ with a moderate bulk velocity $\beta \subset [0.45, 0.55]$. These values give us a Lorentz factor $\Gamma \subset [1.1, 1.2]$ and a Doppler factor $\delta \subset [1.3, 1.7]$.

These results are similar to the values obtained by Pian et al. (1996) which have estimated the Lorentz factor of the plasma responsible for the radio jet to be $\Gamma = 1.2$ and a viewing angle of $\theta \sim 30°$ giving a Doppler factor of $\delta = 1.6$. It is also consistent with the space parameter exploration of Tingay et al. (2002) (See Figure 5 in their work).

The HS is located at 8.6″ from the core position, or 9.9 kpc in projection. Assuming a viewing angle of 30° for the jet we estimate the distance from the center to be 19.8 kpc. The HS exhibits an extended structure, especially in bands 3 and 7 (see Figure 4 and 5). Removing a fitted Gaussian on the HS, the extended structure is extended mainly towards the North direction (see Figure 10), with a projected position angle similar to the jet.

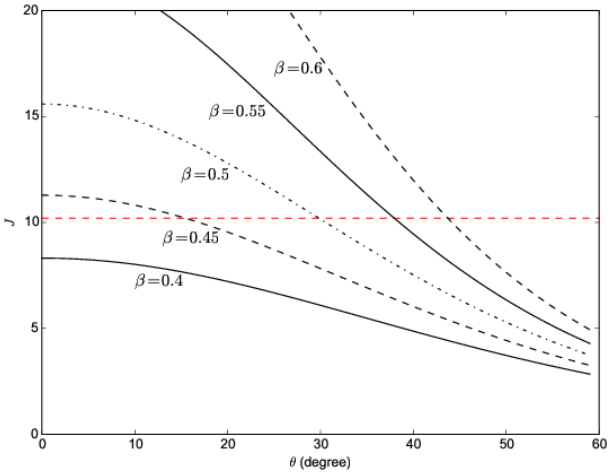

Fig. 9. Jet/counter-jet ratio J for an exponent $p = 2.5$ in function of the viewing angle θ. The curves for different bulk velocity β are plotted. The horizontal line (dashed red line) indicates the flux ratio in *PKS 0521-365*.

Table 8. Flux of regions A and B.

Id	ν_{eff} (GHz)	Flux (A) (mJy)	Flux (B) (mJy)
B367-combined	221.02	5.0	2.3
B6-combined	237.06	3.3	1.6
J0522-364_268_2	247.08	-	1.9
J0522-364_210_1_2	225.43	3.6	1.6
J0522-364_210_3	225.44	4.4	-
B7-combined	336.44	5.3	2.1
J0522-364_108_2	348.58	-	1.6
J0522-364_397_1	344.99	-	1.7
J0522-364_124_1_2	324.15	4.0	-
J0522-364_768_2_3	345.77	5.0	1.6
J0522-364_83_1	348.82	3.3	-
J0522-364_208_1	348.42	3.9	-
J0522-364_223_1	338.19	6.1	-
J0522-364_223_2	338.19	6.7	-
J0522-364_340_1_2	365.28	7.0	

4. (Sub-)millimeter variability

The flux evolution of *PKS 0521-365* in three bands of ALMA, 3, 6 and 7, were measured during nearly 1 year using calibration data of several unrelated scientific projects. The time sampling for each band was irregular and did not allow to study completely the very fast variation (intra-days) or to measure a precise time variation of the individual blobs in the jet given the low signal to noise of the individual measurements, e.g. using a Fourier decomposition in the time domain. Nevertheless, it was possible to disclose important flux variation. On Figure 11 the evolution of the total flux in the three bands is shown. No correction for the frequency was applied but given the spectral index of the core at the different bands (see Table 10) the maximum correction would be in band 7 of the order of 4%.

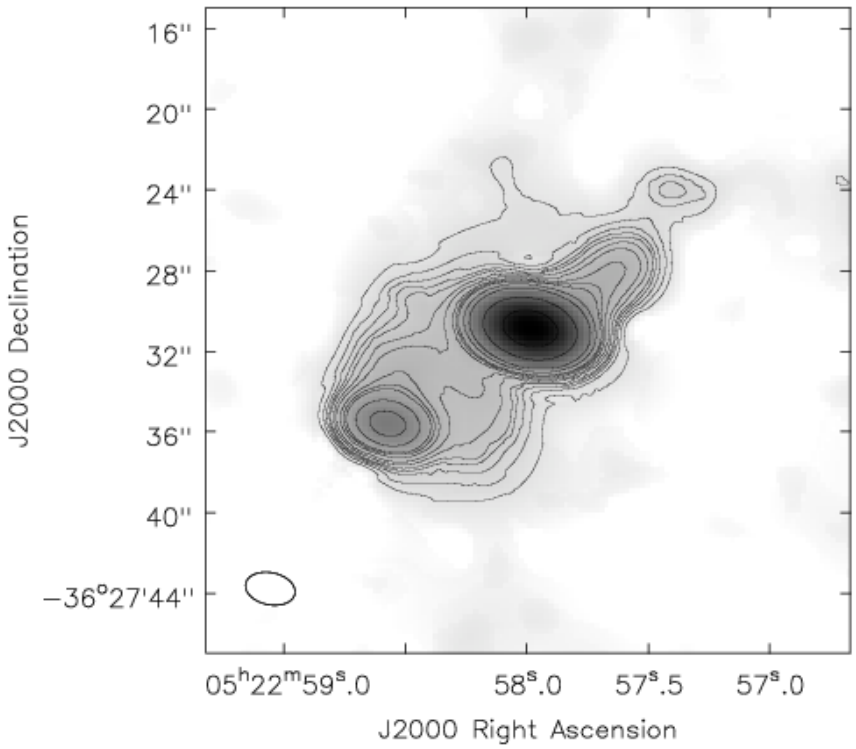

Fig. 4. Continuum emission towards *PKS 0521-365* in band 3 (ν_{eff} = 100.43 GHz) after filtering at 4.5-σ using a WT. The contours are at [3, 5, 7, 9, 11, 15, 20, 30, 40, 50, 100, 200, 1000, 5000]-σ for a RMS noise of 306 μJy.

Table 6. Coordinates (J2000) of some regions in *PKS 0521-365*. See Figure 7.

Region	RA (J2000)	Dec (J2000)
Hot Spot (HS)	05:22:58.58	-36:27:35.6
A	05:22:57.85	-36:27:29.9
B	05:22:57.62	-36:27:27.9

Table 7. Flux of the counter-jet in *PKS 0521-365*.

band	ν_{eff} (GHz)	Flux (mJy)	RMS (mJy)	Comments
3	106.62	15.0	1.0	J0522-364_99_3 uniform weighting
3	104.33	20.0	3.9	J0522-364_99_3 uniform weighting
3	102.40	25.5	4.7	J0522-364_467_1 uniform weighting
6	221.02	0.8	0.16	band 3,6,7 combined and WT filtered
6	237.06	1.8	0.26	band 6 combined and WT filtered
6	225.43	1.2	0.3	J0522-364_210_1_2
6	225.43	3.1	0.7	J0522-364_210_3
7	-	-	-	Not detected

The variability index VI (Ciaramella et al., 2004) was introduced to parametrize the flux variation of a source:

$$VI = \frac{S_{max} - S_{min}}{S_{max} + S_{min}} \quad (5)$$

For each band, the VI of *PKS 0521-365* is then estimated on the sampling period of 1 year to be respectively VI_{B3} = 0.33, VI_{B6} = 0.06 and VI_{B7} = 0.40 (see Table 10). These values of the VI must be considered as lower limit during the year 2012 since the sampling is sparser than the variability in *PKS 0521-365*. The sparse and irregular sampling makes difficult to draw clear conclusions on the variability between the bands. Nevertheless, it seems that the emission in band 3, the lowest frequencies, is more variable than the other two bands.

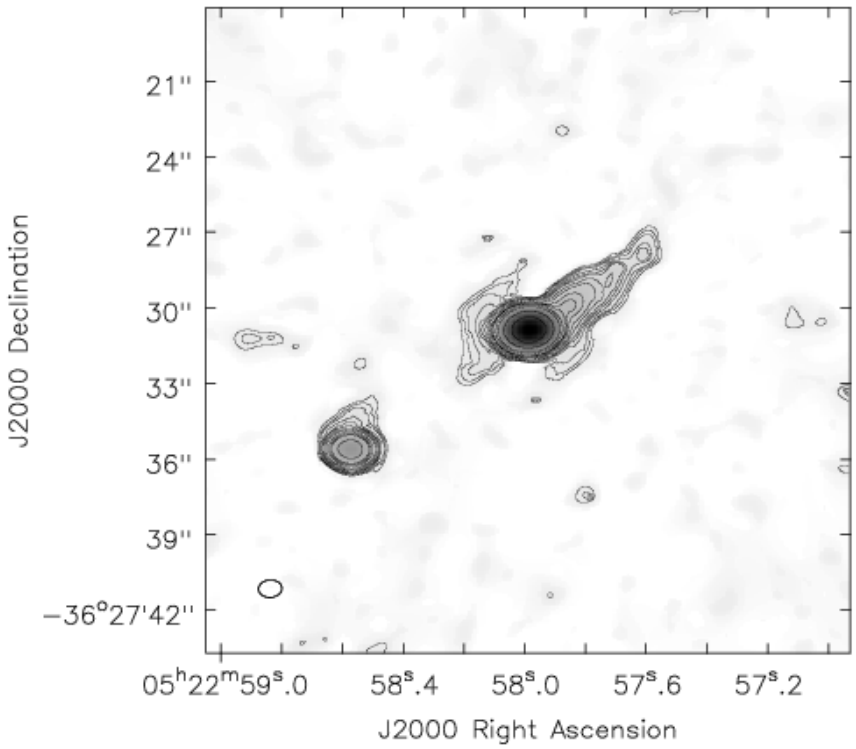

Fig. 5. Continuum emission towards *PKS 0521-365* in band 6 (ν_{eff} = 237.06 GHz) after filtering at 4.5-σ using a WT. The contours are at [3, 4, 5, 7, 9, 11, 15, 20, 30, 40, 50, 100, 200, 1000, 5000]-σ for a RMS noise of 147 μJy.

5. Spectral index

On Table 9 the spectral index is given per dataset. The spectral index was computed measuring the core flux at the 4 basebands of a given dataset (see Figure 12). The mean value of the spectral index was computed for each band (see Table 10) and shows a clear correlation with the frequency with a steepening towards the high frequency, −0.43 in band 7 versus −0.08 in band 3. The time evolution of the spectral index for each band (see Figure 13) shows a very quick change for the spectral index in band 7, which in less than 5 days it can change by more than 0.5 dex. That behavior was already shown at lower frequencies in other blazars (e.g. Venturi et al., 2001).

The dynamic range achieved for the imaging of the different dataset allows to measure the flux of the other components. Since the regions A and B are embedded in the jet emission we take a fixed circular aperture of 1″around the peak emission to estimate the flux. The SED of these components is shown on Figure 14 (HS) and 15 (counter-jet, A and B). The very low value, −2.9, of the spectral index of the counter-jet is not only reflecting the intrinsic flux distribution but as well the relativistic beaming of the jet/counter-jet as discussed before. The HS discloses a steep distribution with a spectral index of −1.6 similar to Hot Spots at high frequency in other radio galaxies (Carilli et al. 1999, Okayasu et al., 1992).

The regions A and B in the radio jet have a different behavior with a flat or even inverted spectrum. We note that because of the spatial resolution necessary to discriminate the regions A and B the spectral index was measured from the band 6 and 7. Figure 15 makes clear the large dispersion of the measurements. The time variation cannot be discarded even if it is not expected. A most likely reason for these variations is the difficulty to extract the flux from a region with a single dataset because of the low dynamic range in the radio jet and the ill-defined location. Despite these issues we can confidently affirm that regions A and B have a relatively flat spectrum in band 6 and 7.

Table 10. Mean values of core spectral index in *PKS 0521-365* and the VI per band without correcting for the spectral dependence.

band	#	α	VI
3	6	-0.08	0.40
6	4	-0.19	0.23
7	13	-0.43	0.48

6. Discussion

6.1. Beamed radio jet

The detection of the jet and counter-jet emission allows to use their ratio, $\Re$, as an alternative beaming indicator assuming no isotropic component in the jet emission (Ghisellini et al. 1993). This beaming indicator is independent of other methods such as the proper motion of blobs and the core to extended radio flux usually used with VLBI observations. Also, the resolution required to detect kinematic motions within the jet by ALMA is difficult to achieve frequently enough to monitor the movement

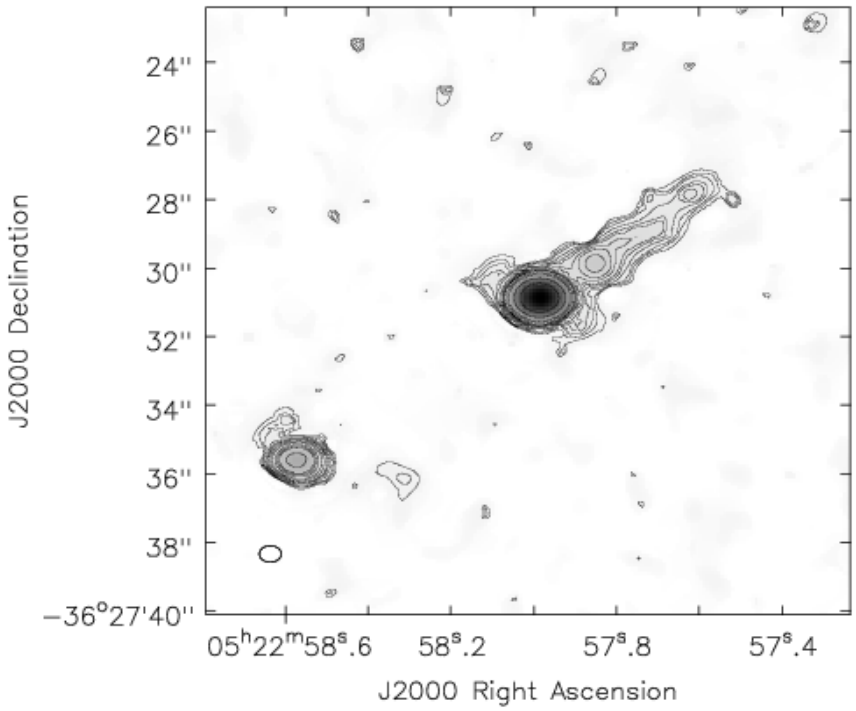

Fig. 6. Continuum emission towards *PKS 0521-365* in band 7 (ν_{eff} = 336.44 GHz) after filtering at 4.5-σ using a WT. The contours are at [3, 4, 5, 7, 9, 11, 15, 20, 30, 40, 50, 100, 200, 1000, 5000]-σ for a RMS noise of 91 μJy.

of blobs within the jet. But taking advantadge of the ALMA sensitivity, the detection of the counter-jet by the stacking approach followed here is a promising avenue at these frequencies. Our derived value for $\Re$ is similar to those values derived from previous VLBI observations. Tingay et al. (1996) found lower limits for $\Re$ in the range of our findings (5.0 and 9.3 at 4.8 GHz, and greater than 2.9 at 8.4 GHz). Further observations by Tingay & Edwards (2002) obtained $\Re > 20$ from the VLBI observations at 5 and 8.4 GHz increasing the previously obtained lower limit given the higher sensitivity of the new VLBI data. Although our result differs in a factor of 2, it is still within the expected range when compared to other highly beamed blazars (Ghisellini et al. 1993). As previously described, from $\Re > 20$ we derived bounded ranges for δ, Γ, β, and θ (see Section 3) which mean values are in good agreement with previous studies, where $\langle\delta\rangle = 1.5$, $\langle\Gamma\rangle = 1.15$, $\langle\theta\rangle = 32.5°$, and $\langle\beta\rangle = 0.5$. In a highly beamed blazar, the ratio $\Re$ get enhanced due to the beaming effect in the jet. Thus, a small value of $\Re$ suggests that we are seeing the true bulk motions in the jet and not emission due to beaming effects. Tingay & Edwards (2002) observations constrain the parameter space to a well defined region which centered the jet angle close to 30° and $\beta \sim 0.5$. These exploration of the $\beta - \theta$ plane also considered the calculations done by Ghisellini et al. (1993) for the Doppler parameter ($\delta > 1$) and Dondi & Ghisellini (1995) ($\delta > 1.3$), which we can now further constrain with our ALMA data. It is no coincidence that our derived parameters lie just inside the box allowed by Tingay & Edwards (2002) in the $\beta - \theta$ plane and is also consistent with the values used for δ. Therefore, we found little support for highly beamed emission in *PKS 0521-365* and thus, though not detected here, it is unlikely that there are super-luminal motions along the jet.

6.2. Double jet, dust or free-free emission

One of the striking results present in the millimeter continuum emisson towards *PKS 0521-365* is an elongated structure nearly perpendicular to the well-defined radio jet (see Fig. 7). In the combined dataset with an effective frequency of 221 GHz that structure has a size of 4.8″, i.e. 5.5 kpc at the distance of *PKS 0521-365*, and a position angle of 72°. The isophote fitting of the R-band image (Falomo, 1994) indicates that this feature is aligned with the major axis of the host galaxy (PA≈ 75°). The thermal (dust) emission or free-free emission from central star forming region or synchrotron emission are then possible explanations for that feature. Previous observations have shown the presence of kpc-scale disk of molecular gas and dust in the center of radio galaxies (Martel et al. 1999, García-Burillo et al. 2007, Ocaña Flaquer et al. 2010). It has been observed as well X-shaped radio sources with normal pairs of active lobes and lower surface brightness wings of emission (Leahy & Parma 1992, Dennett-Thorpe et al. 2002, Cheung 2007). The 15 GHz VLA map shown in Falomo et al. (2009) has a similar angular resolution (∼ 0.5″) to the ALMA data and a RMS noise of 200 μJy which is sufficient to detect the perpendicular feature if it is a synchrotron emission. No hint of an elongated feature along the major axis is visible on the 15 GHz map where all the other features are clearly detected (HS, jet). Boisson et al. (1989) found a nebular line emission with a low surface brightness extending up

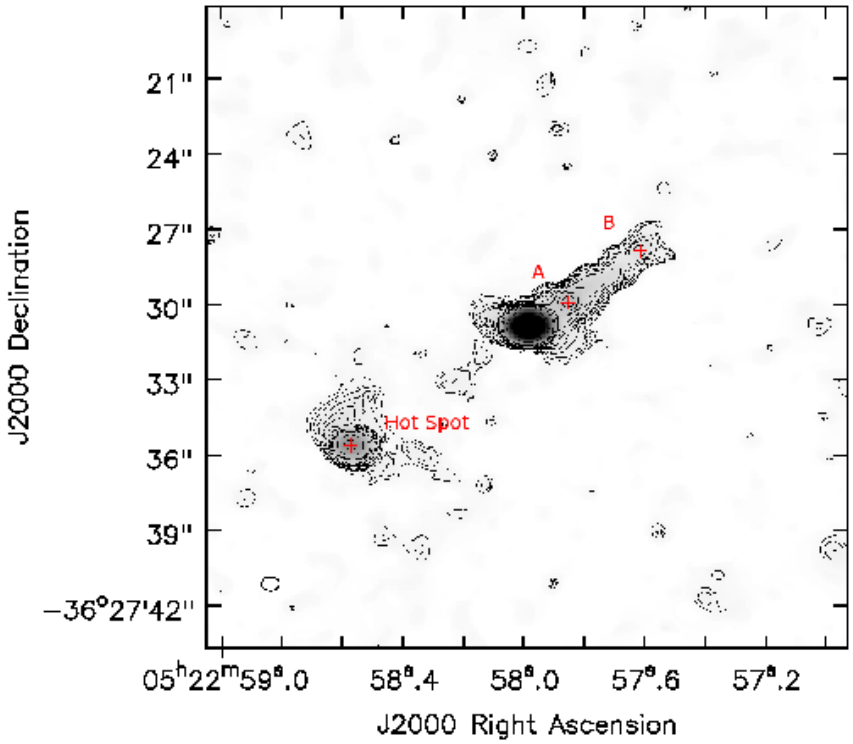

Fig. 7. Continuum emission towards *PKS 0521-365* combining the band 3,6 and 7 data (ν_{eff} = 221.02 GHz) after filtering at 4.5-σ using a WT. The contours are at [3, 4, 5, 7, 9, 11, 15, 20, 30, 40, 50, 100, 200, 1000, 5000]-σ for a RMS noise of 90 μJy. The red crosses point on 3 regions indicated in the text.

to 21 kpc on the opposite side of the radio jet. It does not match spatially with the secondary emission found in band 6 and 7 with ALMA. The spectral index of the emission in the elongated feature between the band 3 and 7 would allow to discriminate between synchrotron and thermal emission since in most of the case the SED slope are negative and positive respectively. The spatial resolution of the current band 3 data does not allow to resolve that feature. The lack of evidence of that feature at 15 GHz favors the dust emission but it will need to be confirmed by observations in band 3 at a higher spatial resolution. In that case the presence of dust in the center of *PKS 0521-365* should be associated with molecular gas that we should be able to detect in CO(1-0) emission or other tracers (Ocaña Flaquer et al. 2010).

7. Conclusions

The blazar *PKS 0521-365* was studied using the ALMA public archive from the projects using that source as a calibrator over more than 11 months. The data in band 3, 6 and 7 were analyzed separately to follow the time variability and combined for each band in a superset at an effective frequency of 221 GHz. To enhance the imaging we applied a wavelet filtering using the "A trous" algorithm to reach a final dynamic range of 47000 in the superset of data. From that analysis we can draw several conclusions about the (sub-)millimeter emission of *PKS 0521-365*:

- The detection of the submillimeter point sources in the field of *PKS 0521-365* are consistent with sub-millimeter galaxy count obtained with similar data using ALMA observations. They show the strong potential of the numerous calibrator fields used in ALMA observations to build a large sample of high-redshift sources over the whole sky spanned by the ALMA scientific projects. A careful analysis of the sources, beyond the scope of this study, would be needed to discard spurious detections.
- The (sub-)millimeter emission of the extended structures in *PKS 0521-365* is detected in band 3, 6 and 7. The Hot Spot was clearly detected at 8″ from the core. The strongly beamed radio jet was detected together with its internal regions (A and B). We detected the presence of a weak counter-jet, symmetric to the radio jet. A roughly perpendicular disky structure is detected in band 3 and 6. That structure may be the relic of a previous jet but a thermal origin cannot be discarded without more observations at higher spatial resolution and frequency.
- The analysis of the time variability shows large variations during the nearly 1 year of measuremens. The irregular sam-

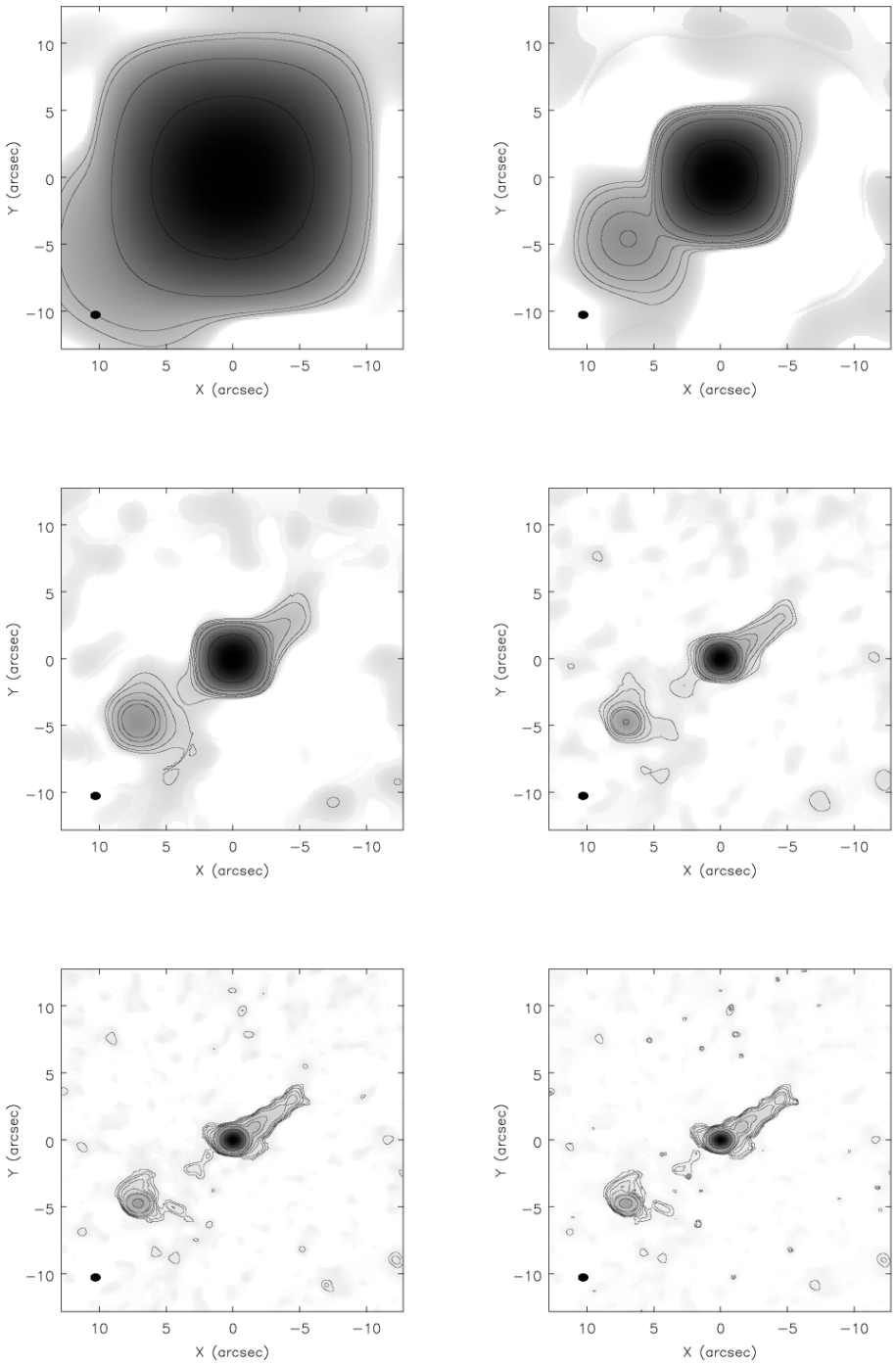

Fig. 8. Image restoration of the combined band 3+6+7 emission using different range of the wavelet filtered planes: planes 6-to-7 (low spatial frequency) on the top left figure to planes 1-to-7 (high spatial frequency) on the bottom right figure. Note that the full reconstruction is achieved with the planes 0-to-7.

pling makes difficult to perform a frequency analysis of the variation. The spectral index variation at the three bands shows large variation reaching 0.4-0.6 dex difference.

– The spectral index analysis indicate a steepening of the SED in the core towards the highest frequencies (band 7) whereas the regions A and B have a quite flat spectrum. The counter-jet displays a very steep SED because of the relativistic beaming in the blazar. Analyzing the data of the jet and counter-jet we were able to put constraint on the Lorentz factor and the viewing angle confirming previous studies at lower frequencies. According to that analysis the Hot Spot would be at a distance of nearly 20 kpc from the core.
– The Hot Spot shows an extended structure apart from its strong central emission. Despite the lower spatial resolution in band 3 it seems to present more extended structures towards the low frequencies.

Table 9. Spectral index of the core of *PKS 0521-365* measured on the basebands.

Id	ν_{eff} (GHz)	α
J0522-364_99_1	104.55	-0.03
J0522-364_99_2	104.33	-0.20
J0522-364_99_3	106.62	0.0
J0522-364_131_1	107.99	0.00
J0522-364_467_1	102.40	-0.06
J0522-364_108_3	93.16	-0.18
J0522-364_268_1	247.08	-0.15
J0522-364_268_2	247.08	-0.05
J0522-364_210_1_2	225.43	-0.28
J0522-364_210_3	225.44	-0.26
J0522-364_108_1	348.58	-0.05
J0522-364_108_2	348.58	-0.51
J0522-364_397_1	344.99	-0.42
J0522-364_124_1_2	324.15	-0.31
J0522-364_83_1	348.82	-0.51
J0522-364_83_2	348.82	-0.22
J0522-364_83_3	348.82	-0.42
J0522-364_208_1	348.42	-1.57
J0522-364_223_1	338.19	-0.37
J0522-364_223_2	338.19	-0.35
J0522-364_340_1_2	365.28	0.03

– Our derived parameters for $\langle\delta\rangle = 1.5$, $\langle\Gamma\rangle = 1.15$, $\langle\theta\rangle = 32.5°$, and $\langle\beta\rangle = 0.5$, are within the range of the constraints imposed by VLBI observation in the $\beta - \theta$ plane indicating that the emission from *PKS 0521-365* is definitely not highly beamed and thus, support minimal super-luminal motions along the jet.

Acknowledgements. We are grateful to the anonymous referee for the very useful comments. M. G. thanks ESO for his studentship. This paper makes use of the following ALMA data: ADS/JAO.ALMA#Id (Id are the project UID indicated in Table 1). ALMA is a partnership of ESO (representing its member states), NSF (USA), and NINS (Japan), together with NRC (Canada) and NSC and ASIAA (Taiwan), in cooperation with the Republic of Chile. The Joint ALMA Observatory is operated by ESO, AUI/NRAO, and NAOJ.

References

Antonucci, R. R. J., Ulvestad, J. S. 1985, ApJ, 294, 158
Bertin, E., Arnouts, S. 1996, A&AS, 117, 393
Best, P. N., Heckman, T. M. 2012, MNRAS, 421, 1569
Bicknell G.V. 1995, ApJS, 101, 29
Bicknell, G. V., Sutherland, R. S.; van Breugel, W. J. M., Dopita, M. A., Dey, A., Miley, G. K. 2000, ApJ, 540, 678
Bijaoui, A. 1991, "The Wavelet Transform", Data Analysis Workshop, 3
Birkinshaw, M., Worrall, D. M., Hardcastle, M. J. 2002, MNRAS, 335, 142B
Blandford, R. D., Rees, M.J. 1978, in Pittsburgh Conferences on BL Lac Objects, ed. A.N. Wolfe (Pittsburgh, University of Pittsburgh Press), p. 328
Boisson, C., Cayatte, V., Sol, H 1989, A&A, 211, 275
Capetti, A., Raiteri, C. M., Buttiglione, S. 2010, A&A, 516, 59
Carvalho, J. C. 1998, A&A, 329, 845
Carilli, C. L., Kurk, J. D., van der Werf, P. P., Perley, R. A., Miley, G. K. 1999, AJ, 118, 2581
Chen, X., Fossati, G., Böttcher, M., Liang, E. 2012, MNRAS, 424, 789
Cheung, C. C. AJ, 133, 2097
Ciaramella, A., Bongardo, C., Aller, H. D., Aller, M. F., De Zotti, G., Lähteenmaki, A., Longo, G., Milano, L., Tagliaferri, R., Teräsranta, H., Tornikoski, M., Urpo, S. 2004, A&A, 419, 485
Danziger, I. J., Fosbury, R. A. E., Goss, W. M., Ekers, R. D. 1979, MNRAS, 188, 415
Danziger, I. J., Bergeron, J., Fosbury, R. A. E., Maraschi, L., Treves, A., Tanzi, E. G. 1983, MNRAS, 203, 565
Dennett-Thorpe, J., Scheuer, P. A. G., Laing, R. A., Bridle, A. H., Pooley, G. G., Reich, W. 2002, MNRAS, 330, 609
Dey, A., van Breugel, W., Vacca, W. D., Antonucci, R. 1997, ApJ, 490, 698
Dondi, L., Ghisellini, G. 1995, MNRAS, 273, 583
Fabian, A.C. 2012, ARA&A, 50, 455
Falcke, H., Wilson, A. S., Simpson, C. 1998, ApJ, 502, 199
Falomo, R. 1994, Messenger, 77, 49
Falomo, R., Pian, E., Treves, A., Giovannini, G., Venturi, T., Moretti, A., Arcidiacono, C., Farinato, J., Ragazzoni, R., Diolaiti, E., Lombini, M., Tavecchio, F., Brast, R., Donaldson, R., Kolb, J., Marchetti, E., Tordo, S. 2009, A&A, 501, 907
Fanaroff, B. L., Riley, J. M. 1974, MNRAS, 167, 31
Fossati, G., Maraschi, L., Celotti, A., Comastri, A., Ghisellini, G. 1998, MNRAS, 299, 433
García-Burillo, S., Combes, F., Neri, R., Fuente, A., Usero, A., Leon, S., Lim, J. A&A, 468, 71
Ghisellini, G., Haardt, F., Fabian, A. C. 1993, MNRAS, 263, 9
Grossmann, A., Morlet, J 1985, in Streit L. (ed) Mathematics+Physics, Lecture on recent results. World Scientific, Singapore
Hatsukade, B., Ohta, K., Seko, Ak., Yabe, K., Akiyama, Masayuki. 2013, ApJL, 769, 27
Keel, W. C. 1986, ApJ, 302, 296
Khalatyan, A., Cattaneo, A., Schramm, M., Gottlöber, S., Steinmetz, M., Wisotzki, L. 2008, MNRAS, 387, 13
Leahy, J. P., Parma, P. 1992, in Extragalactic Radio Sources: From Beams to Jets, ed. J. Roland, H. Sol, & G. Pelletier (Cambridge: Cambridge Univ. Press), 307
Leon, S., Meylan, G., Combes, F. 2000, A&A, 359, 907
Lister, M. L., Marscher, A. P. 1997, ApJ, 476, 572
Macchetto, F., Albrecht, R., Barbieri, C., Blades, J. C., Boksenberg, A., Crane, P., Deharveng, J. M., Disney, M. J.; Jakobsen, P., Kamperman, T. M., King, I. R., Mackay, C. D., Paresce, F., Weigelt, G., Baxter, D., Greenfield, P., Jedrzejewski, R., Nota, A., Sparks, W. B. 1991, ApJ, 369, 55
Maraschi, L., Tavecchio, F. 2003, ApJ, 593, 667
Martel, A. R., Baum, S. A., Sparks, W. B., Wyckoff, E., Biretta, J. A., Golombek, D., Macchetto, F. D., de Koff, S., McCarthy, P. J., Miley, G. K. ApJS, 122, 81
McCarthy, P. J., van Breugel, W., Spinrad, H. Djorgovski, S. 1987, ApJ, 321, 29
Ocaña Flaquer, B., Leon, S., Combes, F., Lim, J. 2010, A&A, 518, 9
Okayasu, R., Ishiguro, M., Tabara, H. 1992, PASJ, 44, 335
Pian, E., Falomo, R., Ghisellini, G., Maraschi, L., Sambruna, R. M., Scarpa, R., Treves, A. 1996, ApJ, 459, 169
Rau, U., Cornwell, T. J. 2011, A&A, 532, 71
Rashed, Y. E., Zuther, J., Eckart, A., Busch, G., Valencia-S., M., Vitale, M., Britzen, S., Muxlow, T. 2013, A&A, 558, 5
Scarpa, R., Falomo, R., Pian, E. 1995, A&A, 303, 730
Scarpa, R., Urry, C., M., Falomo, R., Treves, A. 1999, ApJ, 526, 643
Sparks, W. B., Biretta, J. A., Macchetto, F. 1994, ApJS, 90, 909
Stawarz, Ł., Aharonian, F., Kataoka, J., Ostrowski, M., Siemiginowska, A., Sikora, M. 2006, MNRAS, 370, 981

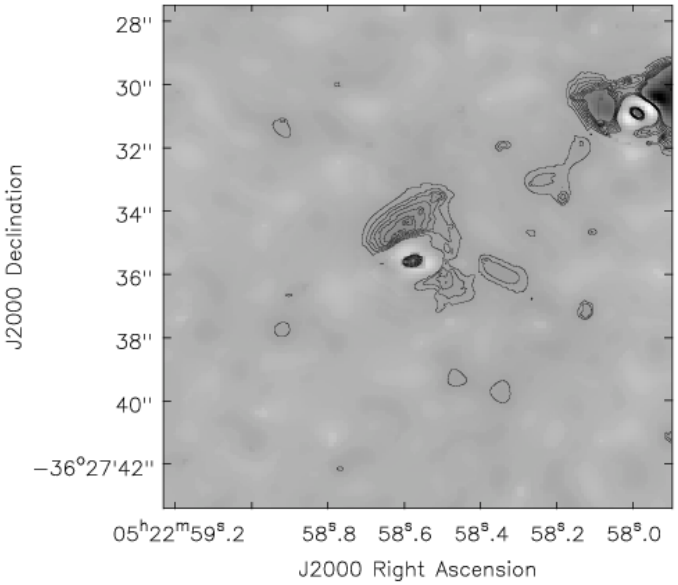

Fig. 10. Emission of the full data set in band 3, 6 and 7. The contours are at [3,4,5,6,7,8,9,10]-σ for a RMS noise of 90 μJy. A Gaussian was fitted and removed from the core emission. The counter-jet is visible at the South-East between the HS and the core.

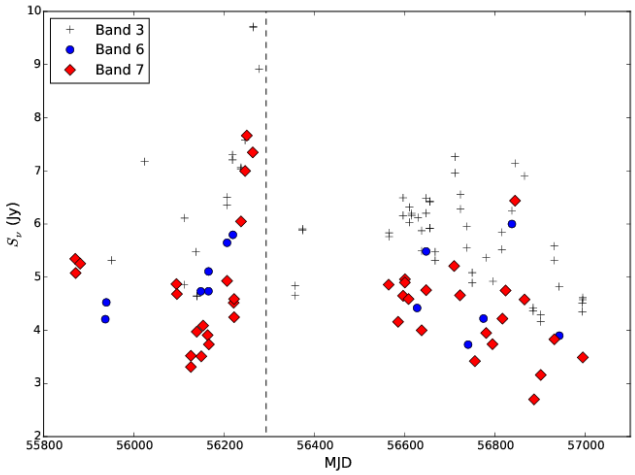

Fig. 11. Flux evolution of the core of *PKS 0521-365*. For the data from the Source Catalogue we removed the Hot Spot flux using the spectral fit.

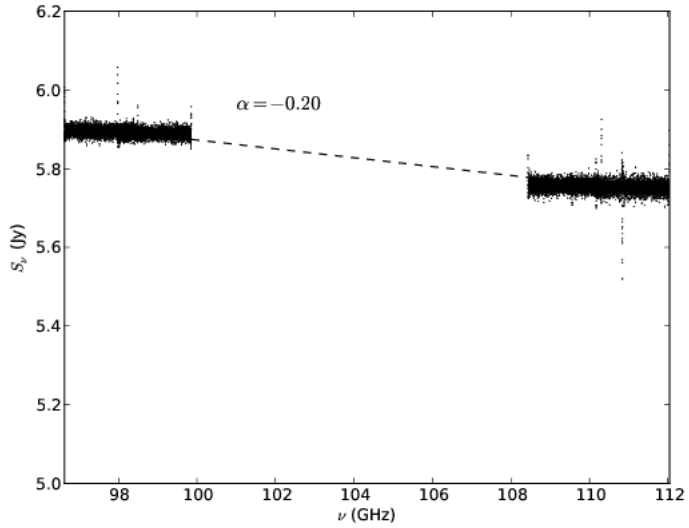

Fig. 12. Spectral index using the 4 simultaneous basebands observed with ALMA. Here is the example of the set J0522-364_99_2. The spectral index fit is indicated by the dashed line.

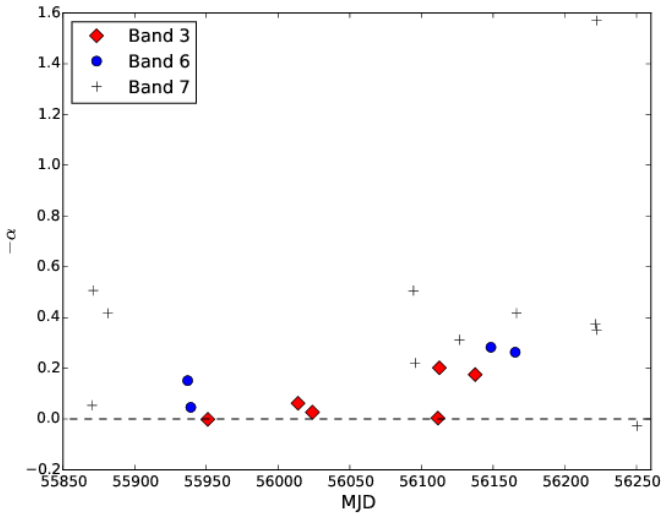

Fig. 13. Evolution of the spectral index α in the core of *PKS 0521-365* vs. MJD. The data from the calibrator monitoring were added to the project data. In that case we remove the Hot Spot flux estimated from the SED fit.

Sturm, E.; González-Alfonso, E., Veilleux, S., Fischer, J., Graciá-Carpio, J.. Hailey-Dunsheath, S., Contursi, A., Poglitsch, A., Sternberg, A., Davies, R., Genzel, R., Lutz, D., Tacconi, L., Verma, A., Maiolino, R., de Jong, J. A. 2011, ApJ, 733, 16

Ulrich, M. H. 1981, A&A, 103, 1

Urry, C. M., Padovani, P. 1995, PASP, 107, 803

Venturi, T., Dallacasa, D., Orfei, A., Bondi, M., Fanti, R., Gregorini, L.. Mantovani, F., Stanghellini, C., Trigilio, C., Umana, G. 2001, A&A, 379, 755

Tavecchio, F., Maraschi, L., Ghisellini, G. 1998, ApJ, 509, 608

Tingay, S. J., Edwards, P. G. 2002, AJ, 124, 652

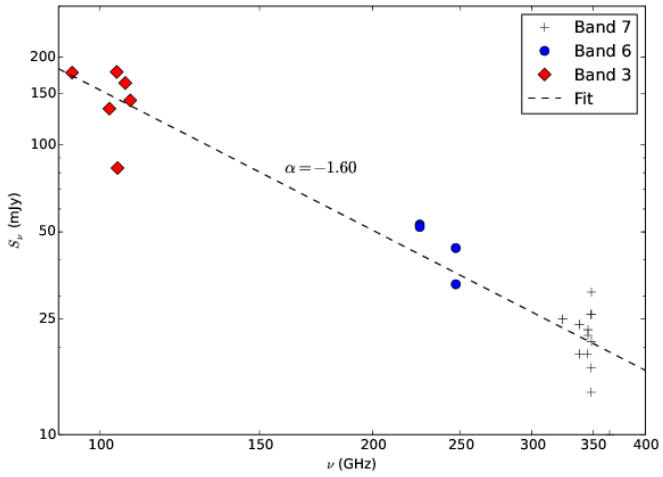

Fig. 14. SED of the Hot Spot in band 3, 6 and 7 and the fit of the spectral index $\alpha = -1.60$.

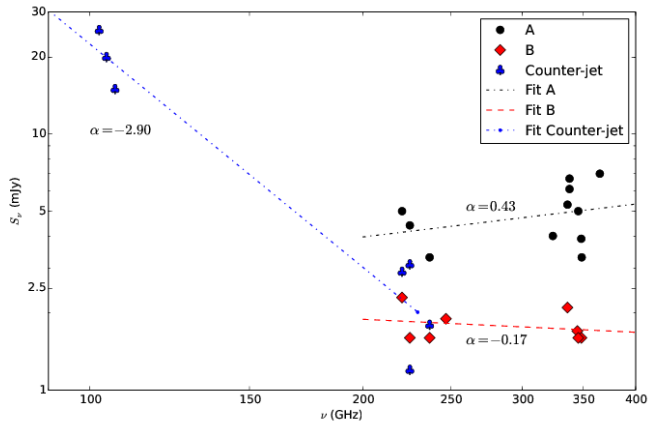

Fig. 15. SED of the measured continuum data in the regions A, B and the counter-jet. A spectral index is fitted on the three regions and indicated in the plot.